sustainability

Article

Enhancing Thermal Performance of Autoclaved Aerated Concrete (AAC) Incorporating Sugar Sediment Waste and Recycled AAC with Phase Change Material-Coated Applications for Sustainable Energy Conservation in Building

Atthakorn Thongtha [1,*], Somchai Maneewan [1] and Ahmad Fazlizan [2]

[1] Department of Physics, Faculty of Science, Naresuan University, Phitsanulok 65000, Thailand; somchaim@nu.ac.th
[2] Solar Energy Research Institute, Universiti Kebangsaan Malaysia, Bangi 43600, Selangor, Malaysia; a.fazlizan@ukm.edu.my
* Correspondence: atthakornt@nu.ac.th; Tel.: +66-5596-3550

Abstract: This research focuses on the integration of waste materials derived from sugar sediment and recycled AAC into the manufacturing process of autoclaved aerated concrete (AAC) to enhance its physical, mechanical, and thermal characteristics. Furthermore, the investigation explores the prospect of augmenting the thermal efficiency of the AAC composite by applying different quantities of paraffin phase change material (PCM) coatings to its external surface. Throughout the thermal testing phase, temperature control was consistently maintained at three distinct levels: 40 °C, 50 °C, and 60 °C, facilitated by a heater serving as the thermal source. The investigation unveiled that the optimal composition encompassed a 10% by weight replacement of sand with recycled AAC content. This formulation resulted in a peak compressive strength of around 5.85 N/mm^2, along with a maximum tobermorite phase ratio of 25.5%. The elevated strength is directly associated with the heightened crystalline nature of the tobermorite phase. The most favorable configuration incorporated a 20 g PCM-coated material, demonstrating remarkable outcomes, including an extension of the time lag by about 55%, a reduction in the decrement factor by around 56.4%, as well as a substantial reduction in room temperature of roughly 15.8% compared to standard AAC without PCM coating, all at a stable temperature of 60 °C. The integration of sustainable waste materials and PCM technology, as illustrated in this study, notably contributes to resource conservation and the advancement of energy-efficient architectural practices.

Keywords: autoclaved aerated concrete; sugar sediment waste; recycled AAC; phase change material; building insulation; sustainable construction material; energy efficiency; waste materials; time lag; compressive strength

check for updates

Citation: Thongtha, A.; Maneewan, S.; Fazlizan, A. Enhancing Thermal Performance of Autoclaved Aerated Concrete (AAC) Incorporating Sugar Sediment Waste and Recycled AAC with Phase Change Material-Coated Applications for Sustainable Energy Conservation in Building. *Sustainability* **2023**, *15*, 14226. https://doi.org/10.3390/su151914226

Academic Editors: Moruf Olalekan Yusuf, Bassam A. Tayeh, Saheed Kolawole Adekunle and Adeshina A. Adewumi

Received: 14 August 2023
Revised: 10 September 2023
Accepted: 18 September 2023
Published: 26 September 2023

1. Introduction

In recent decades, the global demand for electricity consumption in buildings has undergone a striking and unrelenting escalation. The consumption rate surged from 26% to 54% between 1980 and 2010 and projections indicate that this demand will rise to 84% by 2050 [1,2]. This steady and substantial increase in building energy consumption can be attributed to a confluence of factors, including the relentless growth of the global population, the rapid advancement of modern society, and notable improvements in overall quality of life. Hence, maintaining an optimal indoor temperature for comfort, particularly in tropical climates, has become a difficult and important challenge.

Dealing with this issue involves addressing the significant contribution of air-conditioning systems when cooling and heating, which makes up approximately 65% of the overall energy use within constructions [1–3]. One viable solution for curbing energy consumption demands in the construction sector lies in reducing cooling loads by mitigating thermal accumulation and transmission within buildings [4–8]. As such, the utilization of wall insulation materials has shown great promise, particularly in warm and humid climates [8,9]. The emergence of autoclaved aerated concrete (AAC) production in Thailand presents a hopeful direction for advancing sustainable construction practices. AAC stands out for its remarkable ability to achieve approximately 50% energy savings without additional thermal insulation materials, positioning it as a potential key player in energy conservation [10–15]. Its lightweight and highly porous structure, with about 80% volume comprised of pores, provides lower thermal insulating capacities, higher heat resistance, and reduced shrinkage compared to traditional concrete [16–27], contributing to enhanced energy efficiency in buildings.

Numerous strategies have been put forth for mitigating CO_2 emissions in the construction and civil engineering sectors [28,29]. The initial process involves extending the lifespan of concrete through durability enhancements, which indirectly decreases CO_2 emissions. The second strategy centers on the development of low-carbon cement, including magnesium phosphate cement and sulfoaluminate cement. The third approach entails the incorporation of cementitious admixtures, such as fly ash, slag, and other waste materials, as partial substitutes for cement.

To address the growing waste generation while promoting sustainability, researchers explore utilizing various waste materials as components in AAC production. By utilizing residual materials from industrial procedures, including expanded perlite waste (EPW) [15], efflorescent sand and phosphorescent slag [30], iron ore tailings [31], air-cooled slag [32], crushed siliceous stone [33], lead–zinc tailings [34], coal bottom ash [35], copper tailings and blast furnace slag [36], calcium fly ash and natural zeolite [37], waste from sugar sediment [38], and black dust [39,40]. AAC properties are enhanced, leading to economic and environmental benefits [15–27]. For instance, incorporating EPW as a substitute for ground quartz sand reduces thermal conductivity without sacrificing compressive strength [15].

For instance, Wang et al. [31] studied the utilization of tailings from Chengchao Iron Ore Mine in aerocrete. They explored various parameters like cement–lime ratios, silicon-material dosages, and aluminum powder content. Their results offered new prospects for the application of low-silicon iron ore tailings. The introduction of expanded perlite waste (EPW) in lieu of quartz sand resulted in a reduction in thermal conductivity [15]. Increasing EPW weight percentage further reduced thermal conductivity while maintaining the necessary compressive strength up to 10% EPW content. Mostafa et al. [32] investigated replacing lime and sand with air-cooled slag, achieving an optimum compressive strength of approximately 3.8 N/mm^2. Wang et al. [33] examined clayish crushed stone in aerated concrete, revealing the formation of specific compounds during hydration. Li et al. [34] produced aerated concrete using lead–zinc tailings, studying water–binder ratios, casting conditions, and more. Kurama et al. [35] utilized coal bottom ash as aggregate, resulting in 50% coal bottom ash AAC exhibiting 2.78 N/mm^2 strength. Huang et al. [36] explored replacing lime with copper tailings and blast-furnace slag, achieving 0.61 g/cm^3 density and 4.0 N/mm^2 compressive strength. Jitchaiyaphum et al. [37] replaced Portland cement with fly ash and natural zeolite, obtaining lightweight concrete with compressive strengths of 3.65 and 4.51 N/mm^2. Another significant study involved AAC development by replacing sand and lime with sugar sediment waste [38]. Reducing sugar sediment waste weight notably boosted compressive strength, rendering insulation layers unnecessary for AAC building blocks. Optimum black dust in AAC increased thermal efficiency by 25%, delayed heat flow by 25%, cut heat flux by 33%, and lowered room temp by 4.7%, surpassing conventional AAC. Black-powder AAC improves insulation and reduces power consumption [39,40].

Enhancing the thermal efficiency of AAC as insulation has significant potential to fulfill the requirements for reducing energy consumption and fostering energy preservation in the construction domain, while also ensuring economic viability in energy generation.

Integrating phase change material (PCM) into buildings or their systems offers an efficient method to enhance thermal storage and decrease energy usage [41–50]. Research involving PCM in elements like Trombe walls [51,52], wall boards [53,54], windows or shutters [55], ceilings [56,57], and roofs [58–60] has consistently demonstrated lowered energy usage. Researchers have explored diverse strategies to enhance PCM's thermal performance. These include using longitudinal vortex generators for Trombe walls [52], integrating double layers of PCM for indoor comfort, and employing PCM in various structures. PCM composite boards have performed well in summers but less effectively in winters [53]. PCM in gypsum boards and double-glazed windows has boosted heat storage and reduced energy use [54–56]. PCM in ceiling fan-assisted buildings improves comfort and energy demand distribution [57]. PCM used in metal-sheet roofs sustains indoor comfort and reduces heat transfer [58]. Passive cooling approaches, such as cool-colored coatings and PCM, decrease energy requirement for cooling by 8.5% [59] and utilize PCM in conical cement roofs for reducing heat flow by around 39% [60].

As the construction industry increasingly emphasizes eco-friendly waste management and energy efficiency, the utilization of residual materials from industrial processes in AAC mixtures represents a significant step towards creating a sustainable and energy-efficient building material. Therefore, this work investigates the potential of incorporating waste materials from sugar sediment and recycled AAC into AAC production, with the aim of enhancing physical and mechanical properties, including thermal performance. Additionally, the study explores the thermal efficiency of autoclaved lightweight concrete with the optimal combination of sugar sediment waste and recycled AAC by applying varying amounts of paraffin PCM coatings to the exterior AAC surface.

2. Experimental Methodology

2.1. Raw Materials and Fabrication of AAC

The procedure used to conduct experiments in AAC production utilized readily available initial substances, which included aluminum (Al), Portland cement, anhydrite ($CaSO_4$), fine sand (with a size smaller than 90 μm), and lime (CaO). The AAC mixture's makeup comprised aluminum (0.09% in weight), Portland cement (17.87% in weight), anhydrite (2.35% in weight), sugar sediment waste (18.76% in weight), fine sand (43.76% in weight), and lime (17.17% in weight). The sugar sediment waste, being abundantly available and considered a cost-free input, was utilized in the AAC production. Additionally, significant quantities of AAC waste were also accessible, and they were ground into microparticles to create the recycled AAC powder. Different percentages of recycled AAC powder waste (0%, 5%, 10%, 15%, 20%, and 25% by weight) were substituted for fine sand in the AAC mixture (identified as AAC-SR). To start the procedure, the composition of AAC materials was thoroughly mixed. Afterward, water was introduced to the mixture, and the resultant mixture was placed into a mold measuring 20 cm × 20 cm × 100 cm. The fabrication process involved subjecting the mold to a temperature range of 180–190 °C and applying a pressure of 12 bars. Under these temperature and pressure conditions, AAC blocks with the desired properties were created. This process took place at a certified manufacturer, adhering to the Thailand Industrial Standard (TIS) 1505-1998 [61].

2.2. Measurements of Density, Water Absorption, Compressive Strength, Flexural Strength, Thermal Conductivity, and Tobermorite Phase

Following the autoclave experiment procedure, precise dimensions were achieved for the autoclaved AAC samples to ensure consistency in various property assessments. Specifically, specimens measuring 7.5 cm × 7.5 cm × 7.5 cm were prepared to facilitate the measurement of dry density, water absorption, and compressive strength. Additionally, samples with dimensions of 4 cm × 4 cm × 16 cm were employed to assess flexural strength. For the evaluation of dry density and water absorption, a drying process was conducted at 105 °C for 24 h, adhering to the guidelines outlined in ASTM C642-97. Compressive strength and flexural strength assessments followed a similar drying process but were carried out at 75 °C for 24 h, as per the specifications in ASTM C1555-03a. To determine thermal conductivity for AAC-SR, a thermal conductivity tester was utilized as part of the analysis process. For the identification of the tobermorite phase, a crucial indicator of AAC properties, X-ray diffraction (XRD) analysis was employed. Furthermore, scanning electron microscopy (SEM) was utilized to gain insights into the microstructure of the AAC-SR composition and mixtures with varying compositions.

2.3. Thermal Behavior Analysis and Utilization of Phase Change Material

The melting range of phase change temperature significantly affects thermal storage efficiency when using PCM in building envelopes. To study the thermal process characteristics of paraffin PCM, a differential scanning calorimetry (DSC) technique was used, measuring from 0 °C to 80 °C with a heat rate of 0.05 °C/min. For further investigation of thermal behaviors, the AAC with an optimal composition containing sugar sediment waste and recycled AAC, demonstrating excellent mechanical properties, was selected. Subsequently, a uniform area on the outside surface of the improved AAC, measuring 20 cm wide × 60 cm long, was coated with different quantities of paraffin PCM (0 g, 10 g, 20 g, and 30 g), identified as AAC-P, to evaluate the thermal performance.

2.4. Assessing the Thermal Properties of the Modified AAC under Controlled Temperature Conditions

The experimental configuration presented in Figures 1 and 2 was utilized to evaluate the time lag and decrement factors of autoclaved aerated concrete (AAC) that was coated with varying quantities of phase change material (PCM) on its outer surface. The designated area for examination maintained consistent dimensions, measuring 20 cm in width and 60 cm in length. This study encompassed multiple locations, each characterized by different initial AAC thicknesses and diverse AAC layers containing varying amounts of PCM. These particular specimens were subjected to temperatures of 40 °C, 50 °C, and 60 °C, and the temperature-control mechanism of a precision heater was employed throughout the assessment of time lag and decrement factors. These specific temperature levels were chosen to emulate the typical thermal conditions observed in buildings within Thailand, where wall temperatures typically range between 40 °C and 60 °C, as reported in references [62,63].

The setup depicted in Figures 1 and 2 was utilized for evaluating time lag and decrement factors of AAC covered with different quantities of PCM (0 g, 10 g, 20 g, and 30 g) on its external surface. The region covered had uniform dimensions of 20 cm wide × 60 cm long. The study included various spots with varying original AAC thicknesses and AAC layers with distinct PCM contents. These spots were subjected to temperatures of 40 °C, 50 °C, and 60 °C. The temperature control of a heater was precise during the assessment of time lag and decrement factors. The chosen temperature levels mirror typical wall temperatures found in Thai buildings, generally ranging from 40 °C to 60 °C [62,63]. Temperature measurements were conducted using K-type thermocouples with a precision of ±0.5 °C. These thermocouples were affixed to both the outside and inside wall surfaces, ensuring direct contact with the AAC material. Insulation was provided using aluminum foil tape, and thermal paste was applied to enhance the quality of contact. The experiment involved tracking ambient temperature, room temperature, as well as external and internal surface temperatures, all recorded at 2 min intervals for 360 min.

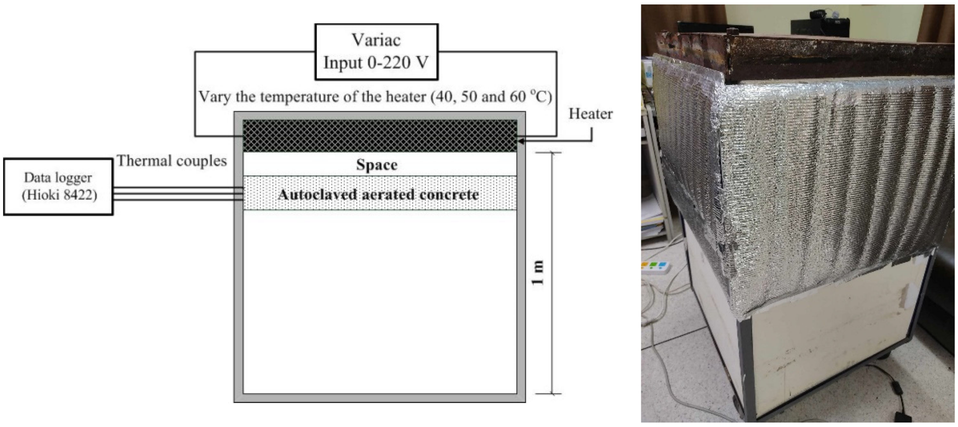

(**a**) (**b**)

Figure 1. (**a**) Schematic diagram illustrating the setup used for the experiment and (**b**) view of the testing room and arrangement of instruments.

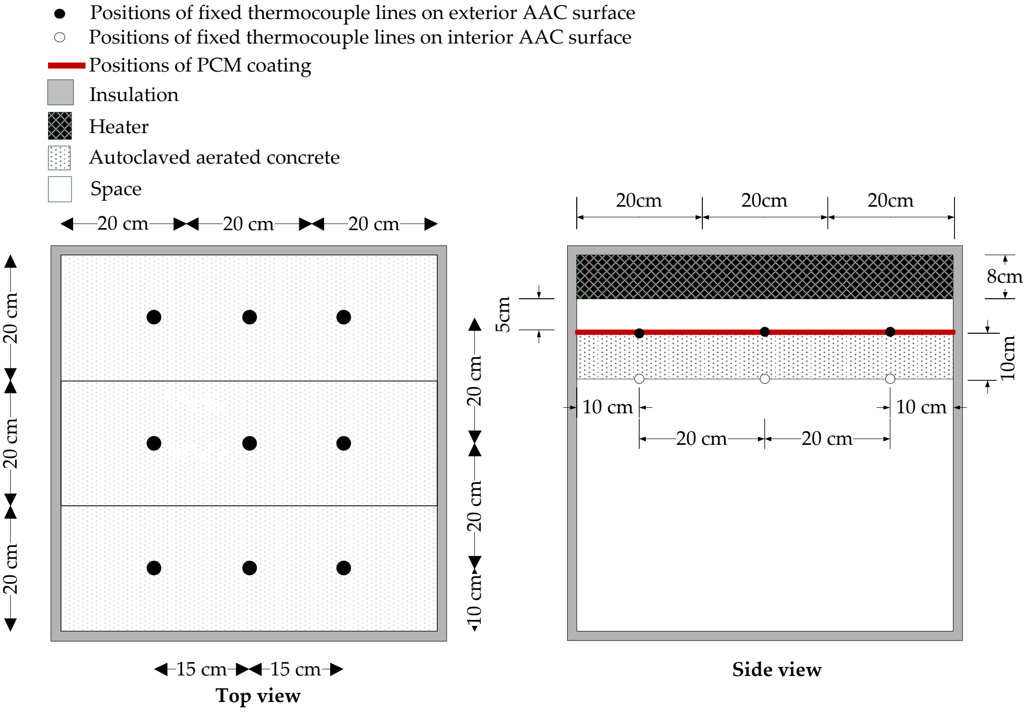

Figure 2. Fixed thermocouples positions for evaluating time lag and decrement factor of specimens.

3. Results and Discussion

3.1. Density, Water Absorption, and Thermal Conductivity

Figure 3 illustrates the impact of varying proportions of recycled AAC content (AAC-SR) on the density and water absorption characteristics of AAC. The density of AAC-SR experienced a slight reduction, shifting from 0.60 g/cm^3 to 0.50 g/cm^3 as the proportion of recycled AAC increased from 0% to 25%, as demonstrated in Figure 3a. These decreased density values corresponded to an increased volume of autoclaved aerated concrete. It is notable that all density measurements were consistently specified within the quality class 4 range (0.51–0.80 g/cm^3) according to the specifications of the Thai Industrial Standard 1505-1998. Simultaneously, the water absorption of AAC-SR indicated a minor increase with the ascent of recycled AAC content. The water absorption rates spanned from 0.39 g/cm^3 to 0.44 g/cm^3 for varying recycled AAC contents between 0% and 25%, as presented in Figure 3b. This trend indicated an inverse relationship between water absorption and density. Furthermore, the volumetric water absorption ratio of all AAC samples conformed to the stipulated criterion of quality class 4 (0.50 g/cm^3) determined in the Thai Industrial Standard 1505-1998.

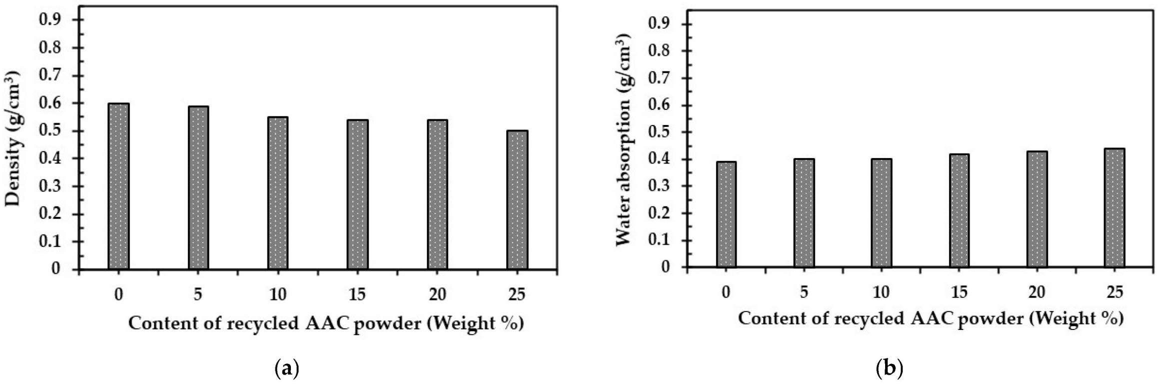

Figure 3. (**a**) Density and (**b**) water absorption of AAC with different contents of fine AAC recycling powder.

The presented paragraph discusses a significant finding regarding the thermal conductivity of AAC-SR, a material comprising recycled AAC content. As the weight proportion of recycled AAC increases from 0% to 25%, the thermal conductivity of AAC-SR notably decreases between 0.124 and 0.104 W/m·K, as indicated by Figure 4. The reduction in thermal conductivity is closely associated with a slight decrease in material density and a minimal rise in water absorption. These changes in density and water absorption can be attributed to the presence of numerous tiny air-filled voids. These micro-sized pores in AAC samples probably play a significant role in lowering thermal conductivity, leading to improved insulation performance by inhibiting the transmission of heat [64]. The noteworthy aspect here is that the inclusion of recycled AAC in the autoclaved aerated concrete mixture enhances its insulating properties. Consequently, heat transfer is reduced, marking an advancement in terms of thermal insulation capabilities. This outcome holds particular importance in achieving improved thermal insulation properties in minimizing heat exchange between the interior and exterior environments, leading to reduced energy consumption for cooling and heating. This finding has significant implications for sustainable energy efficiency in building structures. Ultimately, this contributes to sustainable energy efficiency within buildings and a noteworthy decrease in the peak cooling demand throughout the year.

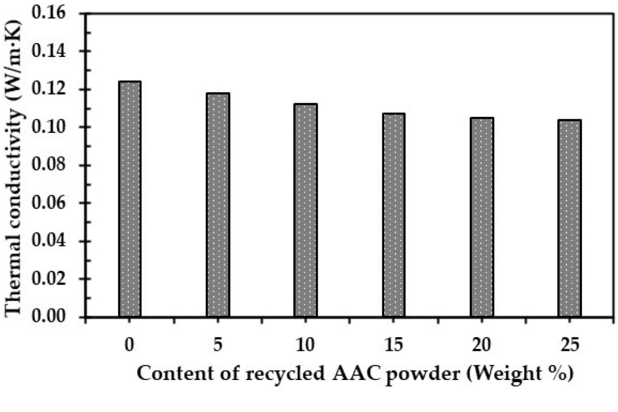

Figure 4. Thermal conductivity of AAC containing sugar sediment with the variation of recycled AAC powder.

3.2. Compressive Strength and Flexural Strength

Figure 5 provides insight into the mechanical strength characteristics of six different AAC compositions, each containing varying quantities of recycled AAC, identified as

AAC-SR. Within this range, the compressive strength of AAC-SR displayed an increase, peaking at 10% recycled AAC content by weight, designated as AAC-SR10. However, beyond this threshold, the compressive strength exhibited a decline, as visually evident in Figure 5a. The highest achieved compressive strength was approximately 5.85 N/mm^2, surpassing not only AAC without recycled AAC but also other materials like coal bottom ash (2.78 N/mm^2) [35], copper tailings and blast furnace slag (4.00 N/mm^2) [36], lightweight concrete with high-calcium fly ash and natural zeolite (4.51 N/mm^2) [37], AAC incorporating black dust waste (4.6 N/mm^2) [39], and AAC designed for ultra-thermal insulation (2.27 N/mm^2) [65]. Traditional AAC generally has a compressive strength of approximately 5.0 N/mm^2.

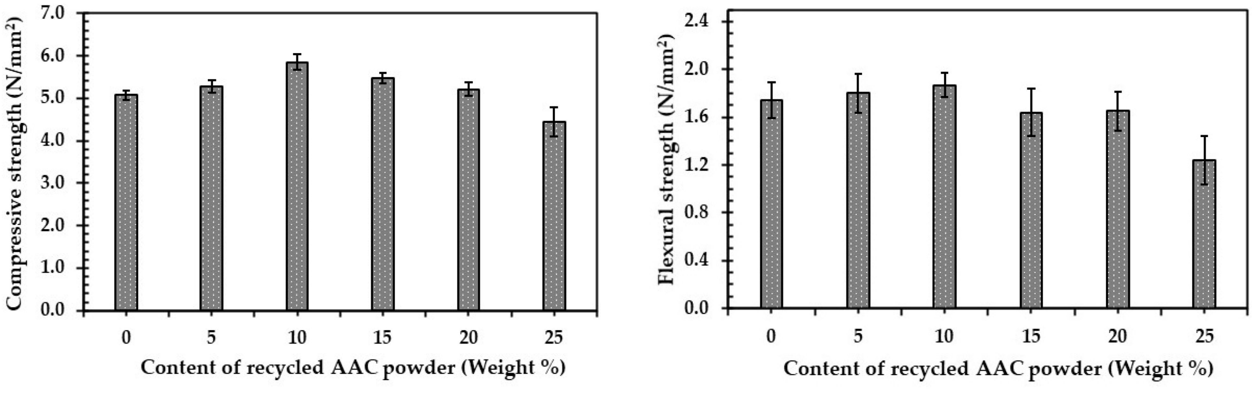

(**a**) (**b**)

Figure 5. (**a**) The measurement of compressive strength and (**b**) the assessment of flexural strength in AAC with the variation between fine sand and AAC recycling powder.

In conclusion, the compressive strength of AAC-SR10 exceeds that of conventional AAC by approximately 17%. Moreover, it significantly surpasses earlier reported achievements that used industrial waste in AAC mixtures, showing enhancements ranging from 29.7% to 157.7%. This substantiates the notion that replacing sand with recycled AAC waste can lead to AAC with exceptional compressive strength. Importantly, these compositions that yield peak compressive strength align with the specifications of the Thai Industrial Standard 1505-1998. This investigation strongly emphasizes the viability of recycling waste AAC as a feasible substitute raw material for the production of AAC.

Figure 5b exhibits the alterations in flexural strength that correspond to different proportions of AAC recycling powder. Following a pattern similar to the trend observed in compressive strength, the flexural strength demonstrated an increase, peaking at a 10% content of recycled AAC powder by weight. Beyond this threshold, the flexural strength gradually decreased. The highest flexural strength, reaching approximately 3.15 N/mm^2, was achieved in the sample containing 10% fine recycling powder by weight, designated as AAC-SR10. This value aligns with the quality class 4 specification (equivalent to ≥30% of the compressive strength) stipulated by the Thai Industrial Standard 1505-1998.

3.3. Phase Formation and Microstructure of AAC

XRD was employed to verify phase formation for the analysis of AAC phase ratios. Figure 6 displays the XRD patterns of the AAC, revealing the presence of calcite, quartz, and tobermorite phases. These three phases within the AAC corresponded to the rhombohedral, hexagonal, and orthorhombic structures, aligned with JCPDS file numbers 02-0629, 05-0490, and 06-0359, respectively. While previous research has noted a correlation between increased compressive and flexural strength and a higher tobermorite phase crystallinity [64–68], a comprehensive investigation into the augmented tobermorite phase ratio within AAC remains limited. To calculate the phase ratios in AAC, the percentages of the three phases were calculated using Equations (1)–(3), which are widely employed in assessing complex structural materials [69]. In these equations, $I_{Calcite}$, I_{Quartz}, and $I_{Tobermorite}$ represent the intensities of the most prominent calcite, quartz, and tobermorite peaks, respectively:

$$\%\text{ ratio of the calcite phase} = \left(\frac{I_{Calcite}}{I_{Quartz} + I_{Tobermorite} + I_{Calcite}}\right) \times 100 \quad (1)$$

$$\%\text{ ratio of the quartz phase} = \left(\frac{I_{Quartz}}{I_{Quartz} + I_{Tobermorite} + I_{Calcite}}\right) \times 100 \quad (2)$$

$$\%\text{ ratio of the tobermorite phase} = \left(\frac{I_{Tobermorite}}{I_{Quartz} + I_{Tobermorite} + I_{Calcite}}\right) \times 100 \quad (3)$$

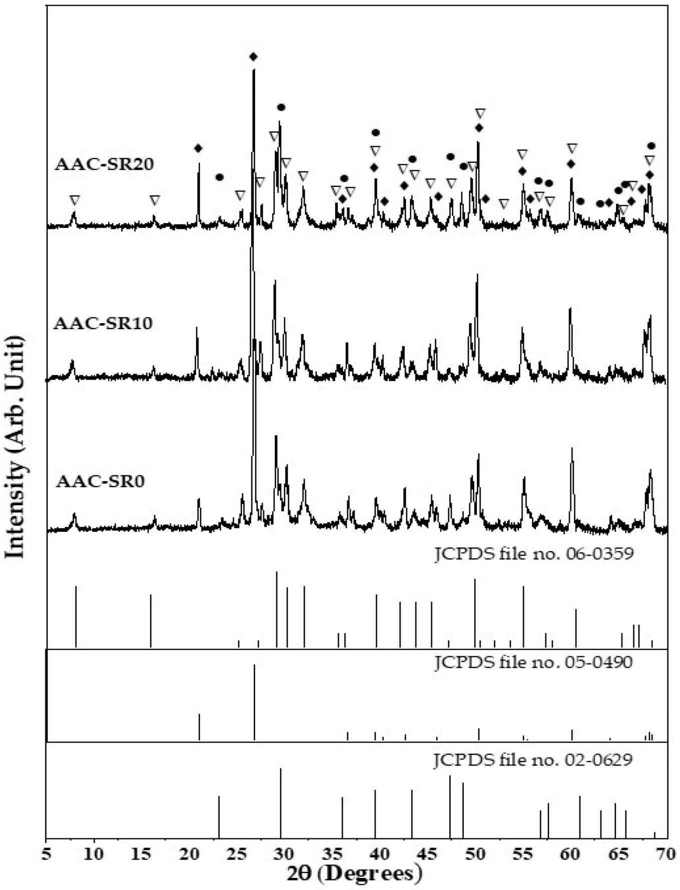

Figure 6. X-ray diffraction patterns of AAC with various mixtures: (∇) tobermorite phase, (♦) quartz phase, and (●) calcite phase.

The composition of calcite, quartz, and tobermorite phases was computed within the AAC-SR0, AAC-SR10, and AAC-SR20 specimens, and these findings are outlined in Table 1. Notably, AAC-SR10 displayed the highest compressive strength among them. A comparative evaluation was conducted between the fabrication of AAC-SR10 and the tobermorite phase proportion within AAC-SR0, serving as the baseline without recycled AAC. The investigation disclosed that the specimens of AAC-SR10, AAC-SR0, and AAC-SR10 showcased the most prominent ratios of calcite, quartz, and tobermorite phases, estimated at approximately 38.1%, 73.2%, and 25.5%, respectively. This heightened ratio of tobermorite and calcite phases, coupled with a relatively reduced quartz phase proportion, was directly associated with improved compressive strength, as demonstrated by the data in Table 1. This observation highlights the shifts in phase distribution within AAC due to the replacing of conventional raw materials, such as sand, with recycled AAC waste. Moreover, this outcome solidifies the notion that an augmentation in the tobermorite phase contributes to enhanced mechanical attributes in AAC, aligning well with previous research findings [64,65].

Table 1. Phase formation ratio of AAC incorporating sugar sediment waste and recycled AAC.

Composition	**Ratio of Phase Formation (%)**		
	Calcite	**Quartz**	**Tobermorite**
AAC-SR0	11.2	73.2	15.6
AAC-SR10	38.1	36.4	25.5
AAC-SR20	32.8	45.3	21.9

In order to illustrate the distinctions in microstructure between AAC-SR0 and the improved composition of AAC (AAC-SR10), Figure 7a,b provides a visual representation of the surface morphology for both AAC-SR0 and AAC-SR10. In both instances, fine needle-like crystalline structures are observed, accompanied by a porous configuration. Within both AAC-SR0 and AAC-SR10, sub-micron needle crystals intricately interlock, forming a robust framework that effectively occupies the spaces between layers. This observation underscores the contribution of the microstructure in both samples to their notable compressive strength. Significantly, AAC-SR10 exhibits larger crystalline structures in comparison to AAC-SR0. To elaborate, the crystallized tobermorite in AAC-SR0 measures between 50–158 nm in width and 1.1–3.8 µm in length, while in AAC-SR10, it exhibits dimensions ranging from 78–164 nm in width and 1.5–4.7 µm in length. The augmentation in crystalline size within AAC-SR10 is closely linked to its higher compressive strength and an elevated presence of the tobermorite phase, aligning with earlier research findings [38,64].

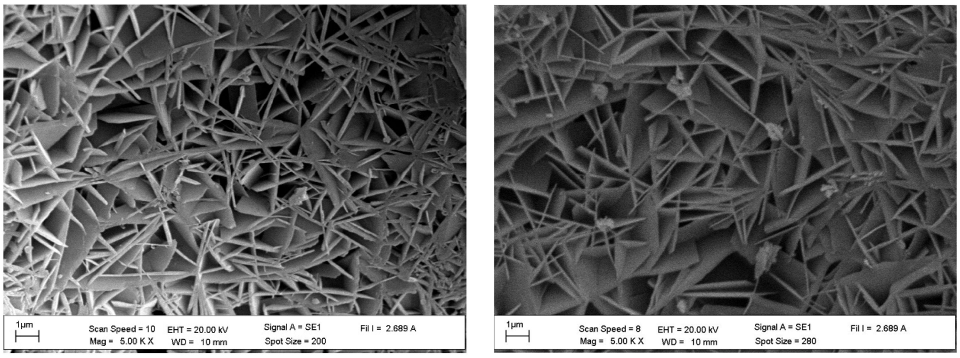

(**a**) (**b**)

Figure 7. SEM photographs at identical levels of magnification depicting (**a**) the surface of AAC-SR0 and (**b**) the surface of AAC-SR10.

3.4. Phase Change Material Behavior

Figure 8 provides a visual representation of the endothermic and exothermic peaks associated with the phase change material, specifically focusing on paraffin. The temperature range under examination spans from 0 °C to 90 °C, encompassing the melting and solidification phases of paraffin PCM. Within this temperature span, we can discern the presence of two distinct endothermic peaks. The initial endothermic peak, a relatively small one, emerges at approximately 49.5 °C and is linked to an enthalpy of 10.05 J/g. This peak marks the initial stage of paraffin melting as it transitions from a solid to a liquid state. Subsequently, as the temperature continues to rise, a broader endothermic peak becomes increasingly prominent at around 59.2 °C. This peak is characterized by a considerably higher enthalpy of 178.07 J/g and signifies the process of fully molten paraffin. It extends from the first endothermic peak, reflecting the broader transition range associated with the melting of paraffin. In the temperature range from 90 °C to 0 °C, we observe the presence of two exothermic peaks. The first exothermic peak materializes at roughly 58.7 °C and is associated with an enthalpy of 169.32 J/g. This peak is attributed to the solidification process of specific paraffin components as they shift from a liquid to a solid state. The second exothermic peak, of a smaller magnitude, is detected around 45.6 °C and exhibits an enthalpy of 16.54 J/g, signifying solidification due to heat release during the cooling process. These findings highlight the suitability of the temperature conditions encompassing the melting and solidification points of paraffin PCM for examining its integration into autoclaved aerated concrete. Moreover, these results hold relevance for potential applications in building walls within the context of Thailand, where typical wall temperatures range from 0 °C to 90 °C, as referenced in [62,63].

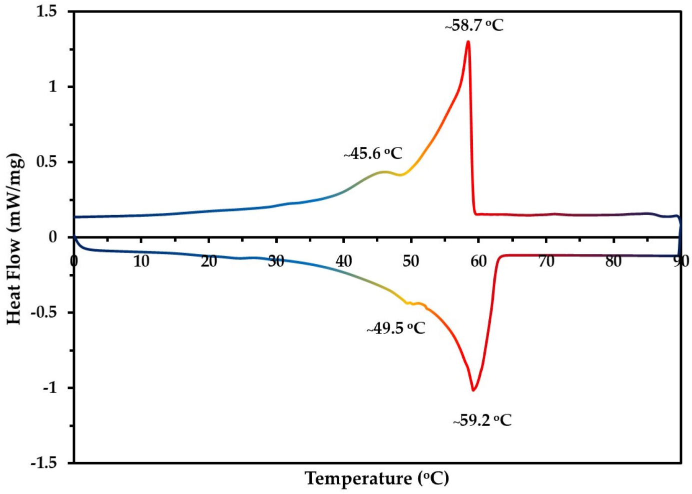

Figure 8. Thermograms derived from DSC analyses of PCM as paraffin.

3.5. Time Lag and Decrement Factor

In order to guarantee the long-term effectiveness of the latent heat storage cycle, stability tests were conducted on the paraffin phase change material (PCM) coated AAC samples to assess its thermal properties through a minimum of 30 repeated heating and cooling cycles. These tests confirmed that the PCM consistently maintained its efficient heat storage and release capabilities. To explore the thermal dynamics of ordinary AAC, as well as AAC-P10, AAC-P20, and AAC-P30, when exposed to controlled temperature environments, concurrent tests were conducted on these four AAC samples with varying levels of PCM coating. In order to assess the response of these materials to temperature fluctuations, a set of simultaneous experiments was carried out, each lasting 360 min at temperatures of 40 °C, 50 °C, and 60 °C. The information gathered during these experiments yielded valuable insights into crucial parameters such as wall temperature (T_s), time lag (ϕ), decrement factor (f), and room temperature (T_r). This extensive dataset is presented in Tables 2–4, offering an in-depth exploration of how different levels of PCM coating content influence these parameters across various temperature conditions. Under the controlled temperature of 40 °C, variations in temperature were detected at various locations, as depicted in Figure 9. Over the course of the 360 min duration, temperature fluctuations were noted at several positions, including the outer wall surface (T_{S0}), a depth of 25 mm within the AAC wall (T_{S25}), a depth of 50 mm within the AAC wall (T_{S50}), the inner wall surface (T_{S75}), and the room temperature (T_r). After the 160 min period, the temperature pattern remained steady at each position. To quantify these findings, average temperatures were evaluated for each location in the AAC samples, focusing on time intervals exceeding 160 min. Notably, samples without PCM coating exhibited average temperatures of about 43.1 °C for the exterior surface, 39.8 °C at a depth of 25 mm, 34.6 °C at a depth of 50 mm, and 31.7 °C at the interior surface. This observation highlighted a connection between AAC thickness and lower temperatures. Interestingly, average temperatures for AAC samples with different levels of PCM coating displayed similarities to those of the uncoated AAC. This information is well documented in Table 2. This experimentation provides valuable insights into the thermal performance of various AAC compositions, particularly in relation to PCM coatings and their effects on temperature fluctuations and stabilization over time.

Table 2. Average wall temperature of AAC with varying PCM at different thickness.

Controlled Temperature (°C)	x (mm)	Average Wall Temperature (°C)			
		AAC	AAC-P10	AAC-P20	AAC-P30
40	0	43.1	43.2	43.1	43.0
	25	39.8	39.2	38.6	38.5
	50	34.6	34.3	33.9	34.0
	75	31.7	31.4	31.2	31.2
50	0	50.2	50.9	51.4	52.0
	25	47.3	47.1	45.6	46.2
	50	40.9	39.0	38.1	38.4
	75	33.7	33.2	32.4	32.5
60	0	59.7	60.7	61.2	61.0
	25	53.5	52.6	51.7	51.8
	50	45.7	44.8	43.0	43.1
	75	34.8	34.2	33.5	33.4

Table 3. Average decrement factor of AAC with different PCM contents.

Temperature (°C)	x (mm)	Decrement Factor			
		AAC	AAC-P10	AAC-P20	AAC-P30
40	0	0	0	0	0
	25	0.340	0.443	0.383	0.356
	50	0.245	0.187	0.152	0.158
	75	0.132	0.184	0.084	0.089
50	0	0	0	0	0
	25	0.357	0.393	0.336	0.362
	50	0.230	0.126	0.118	0.127
	75	0.176	0.094	0.042	0.078
60	0	0	0	0	0
	25	0.382	0.362	0.387	0.395
	50	0.241	0.213	0.108	0.127
	75	0.165	0.110	0.072	0.084

Table 4. Time lag (Φ) of AAC walls with various PCM concentrations at varying thicknesses under controlled 60 °C temperature conditions.

Type of AAC	Time Lag (Φ) at Different Thicknesses (min)			
	0 mm	25 mm	50 mm	75 mm
AAC	0	30	68	80
AAC-P10	0	24	70	92
AAC-P20	0	20	84	124
AAC-P30	0	20	80	120

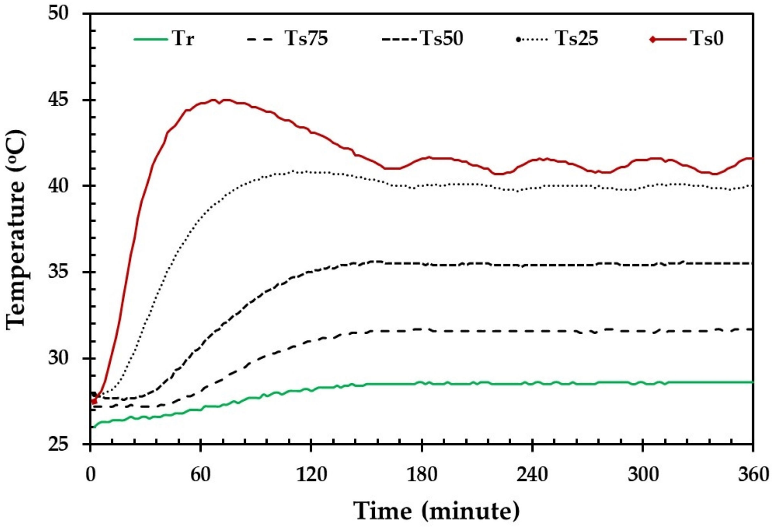

Figure 9. Temperature changes of the AAC wall without PCM coating at 40 °C.

The time lag (ϕ) and decrement factor (f), as established in earlier research [38,63], can be calculated through the utilization of the provided Equations (4) and (5):

$$\phi = \tau_{qi,max} - \tau_{qe,max} \tag{4}$$

$$f = \frac{A_i}{A_e} = \frac{q_{i,max} - q_{i,min}}{q_{e,max} - q_{e,min}} \tag{5}$$

This statement introduces factors used for computing the time lag and decrement factor. $\tau_{qi,max}$ corresponds to the moment when the heat flux on the inner wall surface reaches its maximum, while $\tau_{qe,max}$ signifies the instance when the heat flux on the outer wall surface reaches its maximum. A_i represents the wave amplitudes on the interior wall surface, whereas A_e indicates the amplitudes of the wave on the exterior wall surface. Furthermore, $q_{i,max}$ and $q_{i,min}$ stand for the maximum and minimum heat fluxes of the inner wall surface, respectively, while $q_{e,max}$ and $q_{e,min}$ denote the highest and lowest heat fluxes of the outer wall surface. These parameters play a critical role in understanding the thermal behavior and heat transfer characteristics of the studied materials.

Maintaining the heat source at a constant 60 °C, the time lag exhibited an incremental progression in AAC, gradually extending from 30 to 80 min as the AAC material's thickness increased from 0 to 75 mm. This incremental trend is clearly presented in Table 4. Correspondingly, in the cases of AAC-P10, AAC-P20, and AAC-P30, the time lag also increased proportionally with the expansion of wall thickness from 0 to 75 mm, as substantiated by the data provided in Table 4. Upon reaching a thickness of 75 mm, the resulting time lag values were as follows: approximately 80 min for AAC, 92 min for AAC-P10, 124 min for AAC-P20, and 120 min for AAC-P30. This outcome underscores the notable difference in the time lag behavior among the different PCM-coated AAC samples. Specifically, the time lag for AAC-P20 exhibited a substantial increase of approximately 55.0%, 34.8%, and 3.3% when compared to that of AAC, AAC-P10, and AAC-P30, respectively. This intricate analysis showcases the interplay between AAC thickness and PCM concentration in shaping the temporal dynamics of heat transfer within the studied specimens.

When examining the uncoated AAC material within a controlled environment at 40 °C, there was a noticeable reduction in the decrement factor, decreasing from 0.340 to 0.132 as the AAC wall thickness expanded from 0 to 75 mm. This trend remained consistent as the temperature settings increased to 50 °C and 60 °C. The decrement factor values for these elevated temperatures followed the same pattern observed at 40 °C, aligning with the increasing AAC wall thickness from 0 to 75 mm. This consistent pattern is visually presented in Table 3 for clarity. Shifting attention to the decrement factor of AAC-P10, AAC-P20, and AAC-P30, a similar trend was observed as their values exhibited a decline with an increase in wall thickness within the specified range of 0 to 75 mm. This indicates that the impact of wall thickness on decrement factors remained consistent across different PCM compositions. This corroborative trend is substantiated by the data outlined in Table 3. This observation underscores the inverse correlation between AAC wall thickness and the decrement factor. In simpler terms, augmenting the wall thickness of AAC materials corresponds to a proportional reduction in the decrement factor. This insight underscores the intrinsic connection between wall thickness and the decrement factor, underscoring the pivotal role of material thickness in molding thermal characteristics.

Among the AAC, AAC-P10, AAC-P20, and AAC-P30 compositions tested under different conditions, AAC-P20 demonstrated the lengthiest time lag and the most minimal decrement factor. This phenomenon is notably evident in the behavior of AAC-P20, which modestly extends the duration required for heat transfer through the outside to the inside wall surface and considerably reduces the magnitude of heat oscillations. As a result, AAC-P20 records a comparatively lower room temperature, exhibiting a difference of around 5 °C in contrast to the standard AAC. This observation directly corresponds to the effect of the prolonged time lag, as illustrated in Table 5. Furthermore, the experimental results indicate that the incorporation of sugar sediment waste and recycled AAC in AAC production leads to enhanced mechanical and thermal properties compared to conventional AAC. PCM coatings further amplify the AAC composite’s ability to regulate indoor temperature fluctuations, contributing to energy savings. The study highlights the promising potential of using PCM-coated AAC containing waste materials for sustainable and energy-efficient building applications.

Table 5. Variation in average room temperature of AAC wall with varying levels of coated PCM content.

Temperature (°C)	Average Room Temperature (°C)			
	AAC	**AAC-P10**	**AAC-P20**	**AAC-P30**
40	28.6	28.5	28.4	28.5
50	30.1	30.0	27.6	27.8
60	31.7	30.2	26.7	26.6

4. Conclusions

This study highlights the potential of incorporating sugar sediment waste and recycled AAC materials into AAC production to improve physical and mechanical properties, including thermal performance. Additionally, the use of PCM coatings was explored to improve thermal efficiency. The findings suggest that this approach has the capacity to promote sustainable waste management, optimize resource utilization, and conserve energy in construction. As the proportion of recycled AAC content increased in the mixture, there was a slight reduction in density and a significant reduction in thermal conductivity, along with a slight increase in water absorption. The incorporation of recycled AAC waste led to improved thermal efficiency due to increased air voids within the material. The optimal mixture (AAC-SR10) exhibited superior compressive strength (5.85 N/mm^2), surpassing conventional AAC, and a substantial tobermorite phase ratio (25.5%). These values notably exceeded those obtained from various AAC formulations involving different industrial waste materials.

When PCM coatings, specifically in the optimal content of 20 g (AAC-P20), were applied to the surfaces of AAC containing 10% recycled AAC content (AAC-SR10), it resulted in an approximate 55% delay in heat transfer, a reduction in the decrement factor by approximately 56.4%, and a reduction in room temperature by roughly 15.8% compared to standard AAC at a regulated 60 °C. These improvements in time lag, reduction in the decrement factor, and lowered room temperature collectively lead to a decreased cooling load for the experimental space and significant electricity savings. These findings highlight enhanced insulation properties, resulting in reduced heat transfer and a corresponding achievement of lower room temperatures. Consequently, this innovative approach of incorporating waste materials and PCM-coated AAC could lead to more sustainable and energy-efficient building applications.

Author Contributions: Conceptualization, A.T.; methodology, A.T., S.M. and A.F.; formal analysis, A.T. and S.M.; investigation, A.T., S.M. and A.F.; resources, A.T.; data curation, A.T.; writing—original draft preparation, A.T.; writing—review and editing, A.T. and S.M.; visualization, A.T. and S.M.; supervision, A.T.; project administration, A.T.; and funding acquisition, A.T. All authors have read and agreed to the published version of the manuscript.

Funding: This research was funded by the Thailand Science Research and Innovation (TSRI) through the Fundamental Fund (2022), with support under grant number R2565B077.

Institutional Review Board Statement: Not applicable.

Informed Consent Statement: Not applicable.

Data Availability Statement: MDPI Research Data Policies.

Acknowledgments: The authors express their sincere gratitude to the Thailand Science Research and Innovation (TSRI), the Faculty of Science at Naresuan University, Naresuan University and INSEE Superblock Company Limited for their generous financial support that made this research possible, as well as to our research center for its valuable contributions.

Conflicts of Interest: The authors declare no conflict of interest.

References

1. Ürge-Vorsatz, D.; Cabeza, L.F.; Serrano, S.; Barreneche, C.; Petrichenko, K. Heating and cooling energy trends and drivers in buildings. *Renew. Sustain. Energy Rev.* **2015**, *41*, 85–98. [CrossRef]
2. Adilkhanova, I.; Memon, S.A.; Kim, J.; Sheriyev, A. A novel approach to investigate the thermal comfort of the lightweight relocatable building integrated with PCM in different climates of Kazakhstan during summertime. *Energy* **2021**, *217*, 119390. [CrossRef]
3. Alassaad, F.; Touati, K.; Levacher, D.; Mendili, Y.E.; Sebaibi, N. Improvement of cob thermal inertia by latent heat storage and its implication on energy consumption. *Constr. Build. Mater.* **2022**, *329*, 127163. [CrossRef]
4. Cui, K.; Liang, K.; Chang, J.; Lau, D. Investigation of the macro performance, mechanism, and durability of multiscale steel fiber reinforced low-carbon ecological UHPC. *Constr. Build. Mater.* **2022**, *327*, 126921. [CrossRef]
5. Kumar, D.; Alam, M.; Memon, R.A.; Bhayo, B.A. A critical review for formulation and conceptualization of an ideal building envelope and novel sustainability framework for building applications. *Clean. Eng. Technol.* **2022**, *11*, 100555. [CrossRef]
6. Abbas, H.M.; Jalil, J.M.; Ahmed, S.T. Experimental and numerical investigation of PCM capsules as insulation materials inserted into a hollow brick wall. *Energy Build.* **2021**, *246*, 111127. [CrossRef]
7. Golewski, G.L. The influence of microcrack width on the mechanical parameters in concrete with the addition of fly ash: Consideration of technological and ecological benefits. *Constr. Build. Mater.* **2019**, *197*, 849–861. [CrossRef]
8. Da Cunha, S.R.L.; de Aguiar, J.L.B. Phase change materials and energy efficiency of buildings: A review of knowledge. *J. Energy Storage* **2020**, *27*, 101083. [CrossRef]
9. Pan, J.; Zou, R.; Jin, F. Experimental study on specific heat of concrete at high temperatures and its influence on thermal energy storage. *Energies* **2017**, *10*, 33. [CrossRef]
10. Tao, H.S. *Research for Developing Aerated Concrete by Using Fly Ash with High Calcium of Gehua Power Plant in Hongshan*; Wuhan University of Technology: Wuhan, China, 2004.
11. Huang, L.J.; Wang, H.Y.; Wu, Y.W. Properties of the mechanical in controlled low-strength rubber lightweight aggregate concrete (CLSRLC). *Constr. Build. Mater.* **2016**, *112*, 1054–1058. [CrossRef]
12. Wongsa, A.; Zaetang, Y.; Sata, V.; Chindaprasirt, P. Properties of lightweight fly ash geopolymer concrete containing bottom ash as aggregates. *Constr. Build. Mater.* **2016**, *111*, 637–643. [CrossRef]
13. Dulsang, N.; Kasemsiri, P.; Posi, P.; Hiziroglu, S.; Chindaprasirt, P. Characterization of an environment friendly lightweight concrete containing ethyl vinyl acetate waste. *Mater. Des.* **2016**, *96*, 350–356. [CrossRef]
14. Koronthalyova, O. Moisture storage capacity and microstructure of ceramic brick and autoclaved aerated concrete. *Constr. Build. Mater.* **2011**, *25*, 879–885. [CrossRef]
15. Topcu, I.B.; Isıkdag, B. Effect of expanded perlite aggregate on the properties of lightweight concrete. *J. Mater. Process. Technol.* **2008**, *204*, 34–38. [CrossRef]

16. Beskopylny, A.N.; Shcherban', E.M.; Stel'makh, S.A.; Mailyan, L.R.; Meskhi, B.; Evtushenko, A.; El'shaeva, D.; Chernil'nik, A. Improving the Physical and Mechanical Characteristics of Modified Aerated Concrete by Reinforcing with Plant Fibers. *Fibers* **2023**, *11*, 33. [CrossRef]
17. Thakur, A.; Kumar, S. Mechanical Properties and Development of Light Weight Concrete by Using Autoclaved Aerated Concrete (AAC) with Aluminum Powder. *Mater. Today Proc.* **2022**, *56*, 3734–3739. [CrossRef]
18. Bernard, V.A.R.; Renuka, S.M.; Avudaiappan, S.; Umarani, C.; Amran, M.; Guindos, P.; Fediuk, R.; Ivanovich Vatin, N. Performance Investigation of the Incorporation of Ground Granulated Blast Furnace Slag with Fly Ash in Autoclaved Aerated Concrete. *Crystals* **2022**, *12*, 1024. [CrossRef]
19. Ali, T.; Saand, A.; Bangwar, D.K.; Buller, A.S.; Ahmed, Z. Mechanical and Durability Properties of Aerated Concrete Incorporating Rice Husk Ash (RHA) as Partial Replacement of Cement. *Crystals* **2021**, *11*, 604. [CrossRef]
20. Kumar, M.A.; Prasanna, K.; Chinna Raj, C.; Parthiban, V.; Kulanthaivel, P.; Narasimman, S.; Naveen, V. Bond Strength of Autoclaved Aerated Concrete Manufactured Using Partial Replacement of Flyash with Fibers—A Review. *Mater. Today Proc.* **2022**, *65*, 581–589. [CrossRef]
21. Stepien, A. Analysis of Porous Structure in Autoclaved Materials Modified by Glass Sand. *Crystals* **2021**, *11*, 408. [CrossRef]
22. Soultana, A.; Galetakis, M. Utilization of Quarry Dust and Calcareous Fly Ash for the Production of Lightweight Cellular Micro-Concrete—Synthesis and Characterization. *Buildings* **2020**, *10*, 214. [CrossRef]
23. Matsuno, A.; Kawamoto, K. Assessment of Dispersed Oil Sorption in Oily Wastewater onto Hydrophobized/Oleophilized Autoclaved Aerated Concrete (AAC) Grains. *Environments* **2023**, *10*, 92. [CrossRef]
24. Jasiński, R.; Gąsiorowski, T. Comparative Studies of the Confined Effect of Shear Masonry Walls Made of Autoclaved Aerated Concrete Masonry Units. *Materials* **2023**, *16*, 5885. [CrossRef]
25. Zou, D.; Que, Z.; Cui, W.; Wang, X.; Guo, Y.; Zhang, S. Feasibility of recycling autoclaved aerated concrete waste for partial sand replacement in mortar. *J. Build. Eng.* **2022**, *52*, 104481. [CrossRef]
26. Volk, R.; Steins, J.J.; Stemmermann, P.; Schultmann, F. Comparison of different post-demolition autoclaved aerated concrete (AAC) recycling options. *IOP Conf. Ser. Earth Environ. Sci.* **2022**, *1078*, 012074. [CrossRef]
27. Grzyb, K.; Jasiński, R. Research on the Behavior of Stiffening Walls in Single-Storey Buildings Made of Autoclaved Aerated Concrete (AAC) Masonry Units. *Materials* **2022**, *15*, 7404. [CrossRef]
28. Cui, K.; Lu, D.; Jiang, T.; Zhang, J.; Jiang, Z.; Zhang, G.; Chang, J.; Lau, D. Understanding the role of carbon nanotubes in low carbon sulfoaluminate cement-based composite. *J. Clean. Prod.* **2023**, *416*, 137843. [CrossRef]
29. Cui, K.; Liang, K.; Jiang, T.; Zhang, J.; Lau, D.; Chang, J. Understanding the role of carbon nanotubes in low carbon concrete: From experiment to molecular dynamics. *Cem. Concr. Compos.* **2023**, *142*, 105189. [CrossRef]
30. Ma, B.G.; Zheng, X. Study on a new kind of aerated concrete containing efflorescence sand-phosphorus slag-lime. *J. Build. Mater.* **1999**, *2*, 223–228.
31. Wang, Y.; Yin, J.; Chen, J.C.; Peng, C.Q. Aerocrete made with low silicon tailings of Cheng Chao iron ore mine. *J. Wuhan Univ. Technol. Mater. Sci.* **2000**, *15*, 58–62.
32. Mostafa, N.Y. Influence of air-cooled slag on physicochemical properties of autoclaved aerated concrete. *Cem. Concr. Res.* **2005**, *35*, 1349–1357. [CrossRef]
33. Wang, Q.K.; Chen, Y.Z.; Li, F.X.; Sun, T.; Xu, B.B. Microstructure and properties of silty siliceous crushed stone-lime aerated concrete. *J. Wuhan Univ. Technol. Mater. Sci.* **2006**, *21*, 17–20.
34. Li, F.X.; Chen, Y.Z.; Long, S.Z. Experimental investigation on aerated concrete with addition of lead-zinc tailings. *J. Southwest Jiaotong Univ.* **2008**, *43*, 810–815.
35. Kurama, H.; Topcu, I.B.; Karakurt, C. Properties of the autoclaved aerated concrete produced from coal bottom ash. *J. Mater. Process. Technol.* **2009**, *209*, 767–773. [CrossRef]
36. Huang, X.Y.; Ni, W.; Cui, W.H.; Wang, Z.J.; Zhu, L.P. Preparation of autoclaved aerated concrete using copper tailings and blast furnace slag. *Constr. Build. Mater.* **2012**, *27*, 1–5. [CrossRef]
37. Jitchaiyaphum, K.; Sinsiri, T.; Jaturapitakkul, C.; Chindaprasirt, P. Cellular lightweight concrete containing high-calcium fly ash and natural zeolite. *Int. J. Miner. Metal. Mater.* **2013**, *20*, 462–471. [CrossRef]
38. Thongtha, A.; Maneewan, S.; Punlek, C.; Ungkoon, Y. Investigation of the compressive strength, time lags and decrement factors of AAC-lightweight concrete containing sugar sediment waste. *Energy Build.* **2014**, *84*, 516–525. [CrossRef]
39. Maneewan, S.; Janyoosuk, K.; Hoy-Yen, C.; Thongtha, A. Incorporating black dust into autoclaved aerated concrete wall for heat transfer reduction. *J. Met. Mater. Miner.* **2019**, *29*, 82–87.
40. Mano, C.; Thongtha, A.; Maneewan, S.; Punlek, C. Improvement of the thermal efficiency of autoclaved aerated concrete by black powder. *ScienceAsia* **2021**, *47S*, 76–82. [CrossRef]
41. Kumar, D.; Alam, M.; Sanjayan, J.; Harris, M. Comparative analysis of form-stable phase change material integrated concrete panels for building envelopes. *Case Stud. Constr. Mater.* **2023**, *18*, e01737. [CrossRef]
42. Kumar, D.; Alam, M.; Doshi, A.J. Investigating the influence of thermal conductivity and thermal storage of lightweight concrete panels on the energy and thermal comfort in residential buildings. *Buildings* **2023**, *13*, 720. [CrossRef]
43. Ramakrishnan, S.; Sanjayan, J.; Wang, X. Experimental research on using form-stable PCM-integrated cementitious composite for reducing overheating in buildings. *Buildings* **2019**, *9*, 57. [CrossRef]

44. Liu, X.; Kang, W.; Li, X.; Zeng, L.; Li, Y.; Wang, Q.; Zhang, C. Solid-state mechanochemistry advancing two-dimensional materials for lithium-ion storage applications: A mini review. *Nano Mater. Sci.* **2023**, *5*, 210–227. [CrossRef]
45. Yang, T.; Niu, Y.; Liu, Q.; Xu, M. Cathode host engineering for non-lithium (Na, K, and Mg) sulfur/selenium batteries: A state-of-the-art review. *Nano Mater. Sci.* **2023**, *5*, 119–140. [CrossRef]
46. Wang, H.; Fu, F.; Huang, M.; Feng, Y.; Han, D.; Xi, Y.; Xiong, W.; Yang, D.; Niu, L. Lignin-based materials for electrochemical energy storage devices. *Nano Mater. Sci.* **2023**, *5*, 141–160. [CrossRef]
47. Hui, Z.; An, J.; Zhou, J.; Huang, W.; Sun, G. Mechanisms for self-templating design of micro/nanostructures toward efficient energy storage. *Exploration* **2022**, *2*, 20210237. [CrossRef]
48. He, X.; Zhuo, S.; Tian, L.; Qiao, M.; Lei, X.; Zhang, H.; Zhang, Q. Nanoemulsion-directed assembly of hierarchical ZnS@C nanospheres with penetrating pores for sodium storage. *Battery Energy* **2023**, *2*, 20230001. [CrossRef]
49. Wang, J.; Liu, X.; Xu, Q.; Luo, Q.; Xuan, Y. MXene reconciles concurrent enhancement of thermal conductivity and mechanical robustness of SiC-based thermal energy storage composites. *DeCarbon* **2023**, *1*, 100005. [CrossRef]
50. Chen, X.; Xu, J.; Li, Y.; Gao, Y.; Wang, G. Integrating multiple energy storage in 1D–2D bridged array carbon-based phase change materials. *SusMat* **2023**, *3*, 510–521. [CrossRef]
51. Yin, Q.; Liu, H.; Zhou, T. Citespace-based visualization analysis on the trombe wall in solar buildings. *Sustainability* **2023**, *15*, 11502. [CrossRef]
52. Sergei, K.; Shen, C.; Jiang, Y. A review of the current work potential of a Trombe wall. *Renew. Sustain. Energy Rev.* **2020**, *130*, 109947. [CrossRef]
53. Wang, H.; Lu, W.; Wu, Z.; Zhang, G. Parametric analysis of applying PCM wallboards for energy saving in high-rise lightweight buildings in Shanghai. *Renew. Energy* **2020**, *145*, 52–64. [CrossRef]
54. Rai, A.C. Energy performance of phase change materials integrated into brick masonry walls for cooling load management in residential buildings. *Build. Environ.* **2021**, *199*, 107930. [CrossRef]
55. Li, D.; Wu, Y.; Liu, C.; Zhang, G.; Arıcı, M. Energy investigation of glazed windows containing Nano-PCM in different seasons. *Energy Convers. Manag.* **2018**, *172*, 119–128. [CrossRef]
56. Yang, S.; Zhang, Y.; Zhao, Y.; Felipe Torres, J.; Wang, X. PCM-based ceiling panels for passive cooling in buildings: A CFD modelling. *Energy Build.* **2023**, *285*, 112898. [CrossRef]
57. Alizadeh, M.; Sadrameli, S.M. Indoor thermal comfort assessment using PCM based storage system integrated with ceiling fan ventilation: Experimental design and response surface approach. *Energy Build.* **2019**, *188–189*, 297–313. [CrossRef]
58. Dardouri, S.; Tunçbilek, E.; Khaldi, O.; Arıcı, M.; Sghaier, J. Optimizing PCM integrated wall and roof for energy saving in building under various climatic conditions of Mediterranean region. *Buildings* **2023**, *13*, 806. [CrossRef]
59. Hu, J.; Yu, X. Adaptive building roof by coupling thermochromic material and phase change material: Energy performance under different climate conditions. *Constr. Build. Mater.* **2020**, *262*, 120481. [CrossRef]
60. Yu, J.; Yang, H.; Tao, J.; Zhao, J.; Luo, Y. Performance evaluation and optimum design of ventilation roofs with different positions of shape-stabilized PCM. *Sustainability* **2023**, *15*, 8721. [CrossRef]
61. *TIS 1505-2541*; Autoclaved Aerated Lightweight Concrete Elements. Thai Industrial Standards Institute: Bangkok, Thailand, 1998.
62. Punlek, C.; Maneewan, S.; Thongtha, A. Phase change material coating on autoclaved aerated lightweight concrete for cooling load reduction. *Mater. Sci.* **2017**, *23*, 145–149. [CrossRef]
63. Thongtha, A.; Khongthon, A.; Boonsri, T.; Chan, H.Y. Thermal effectiveness enhancement of autoclaved aerated concrete wall with PCM-contained conical holes to reduce the cooling load. *Materials* **2019**, *12*, 2170. [CrossRef] [PubMed]
64. Ungkoon, Y.; Sittipunt, C.; Namprakai, P.; Jetipattaranat, W.; Kim, K.S.; Charinpanitkul, T. Analysis of microstructure and properties of autoclaved aerated concrete wall construction materials. *J. Ind. Eng. Chem.* **2007**, *13*, 1103–1108.
65. Yang, R.C.; Zhu, J.P.; Wu, Z.S.; Wu, Z.R.; Li, M.; Peng, C.H. Thermal insulation and strength of autoclaved light concrete. *J. Wuhan Univ. Technol. Mater. Sci. Ed.* **2011**, *26*, 132–136. [CrossRef]
66. Narayanan, N.; Ramamurthy, K. Microstructural investigations on aerated concrete. *Cem. Concr. Res.* **2000**, *30*, 457–464. [CrossRef]
67. Narayanan, N.; Ramamurthy, K. Structure and properties of aerated concrete cement: A review. *Cem. Concr. Compos.* **2000**, *22*, 321–329. [CrossRef]
68. Kus, H.; Carlsson, T. Microstructural investigations of naturally and artificially weathered autoclaved aerated concrete. *Cem. Concr. Res.* **2003**, *33*, 1423–1432. [CrossRef]
69. Thongtha, A.; Angsukased, K.; Bongkarn, T. Fabrication of $(Ba_{1-x}Sr_x)(Zr_xTi_{1-x})O_3$ ceramics prepared using the combustion technique. *Smart Mater. Struct.* **2010**, *19*, 124001. [CrossRef]